Electronic Supplementary Material (ESI) for Energy & Environmental Science.
This journal is © The Royal Society of Chemistry 2024

Supplementary information

Ballistic Electrolyte Ions Transport with Undisturbed Pathways for Ultrahigh-Rate Electrochemical Energy Storage Devices

Situo Cheng[1#], Zhen Cao[2#], Yupeng Liu[1], Junli Zhang[1], Luigi Cavallo[2], Erqing Xie[1], and Jiecai Fu[1]*

[1]Key Laboratory for Magnetism and Magnetic Materials of the Ministry of Education, School of Physical Science and Technology, Lanzhou University, Lanzhou 730000, P. R. China

[2]KAUST Catalysis Center, King Abdullah University of Science and Technology (KAUST), Thuwal 23955-6900, Saudi Arabia

#S.C. and Z.C. contributed equally.

*Corresponding authors

E-mail address: fujc@lzu.edu.cn (Jiecai Fu).

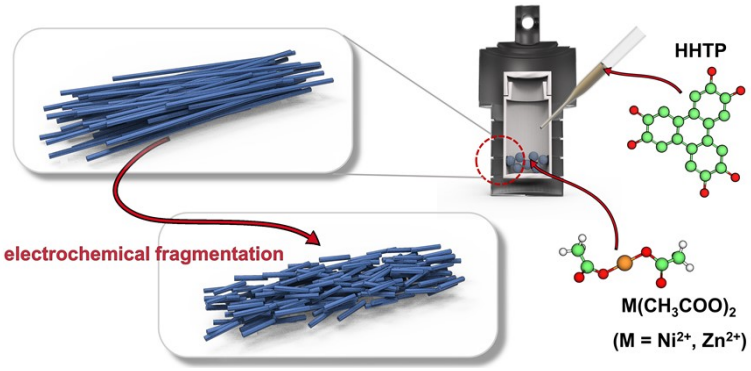

Fig. S1 Schematic diagram of Zn/Ni-CAT synthesis and electrochemical fragmentation process of as-synthesized Zn-CAT.

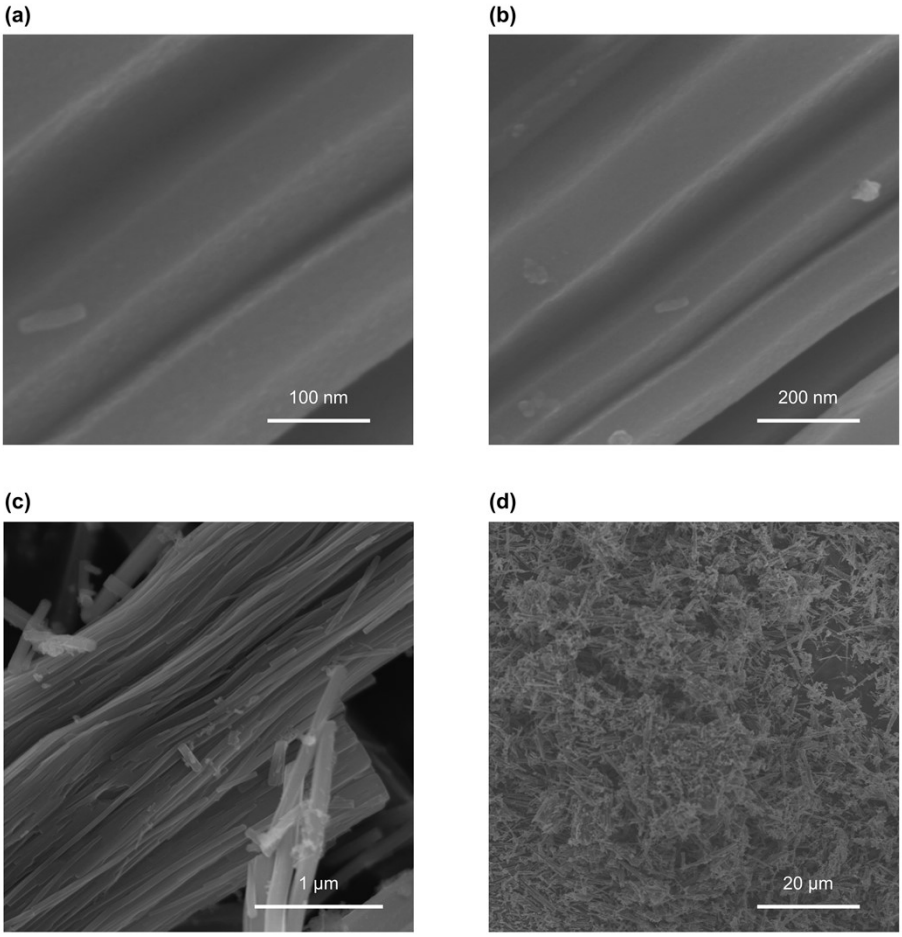

Fig. S2 SEM images of the pristine Zn-CAT.

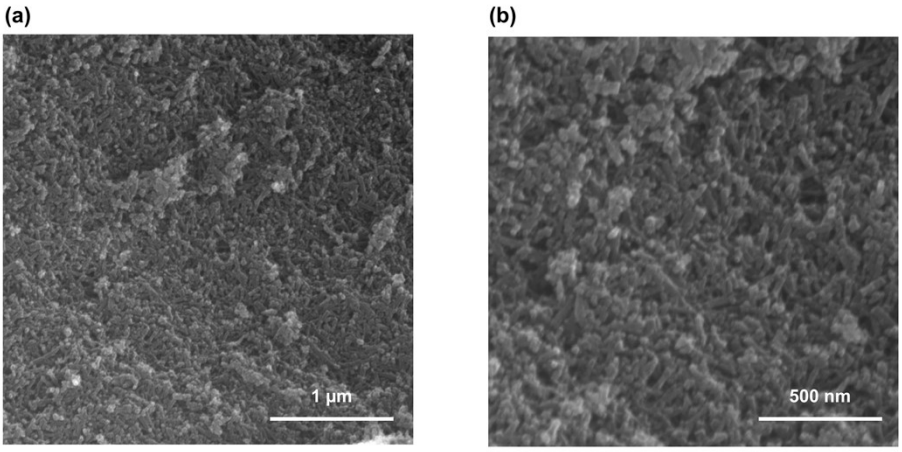

Fig. S3 SEM images of the Ni-CAT.

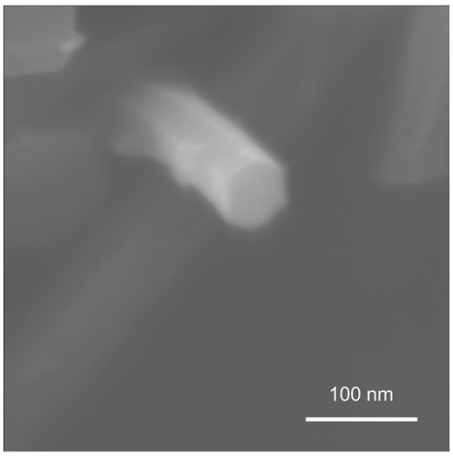

Fig. S4 HR-SEM images of the Ni-CAT.

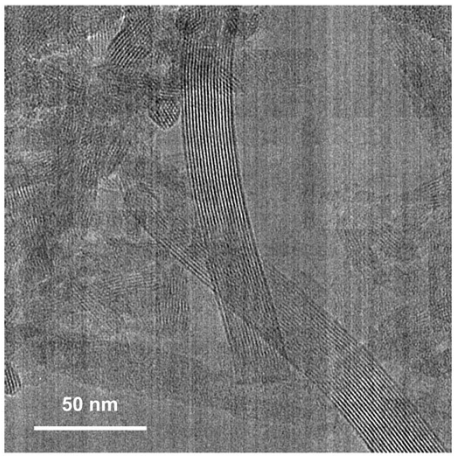

Fig. S5 HR-TEM image of the Ni-CAT.

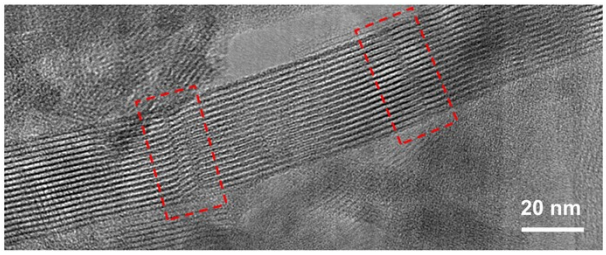

Fig. S6 HR-TEM image of the Ni-CAT.

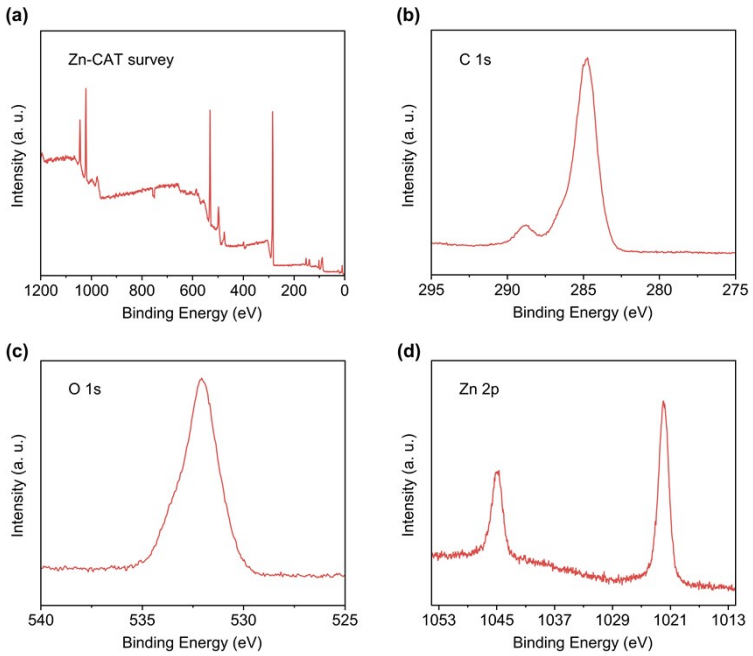

Fig. S7 XPS spectra of Zn-CAT. (a) Zn-CAT survey and the corresponding (b) C 1s, (c) O 1s and (d) Zn 2p region.

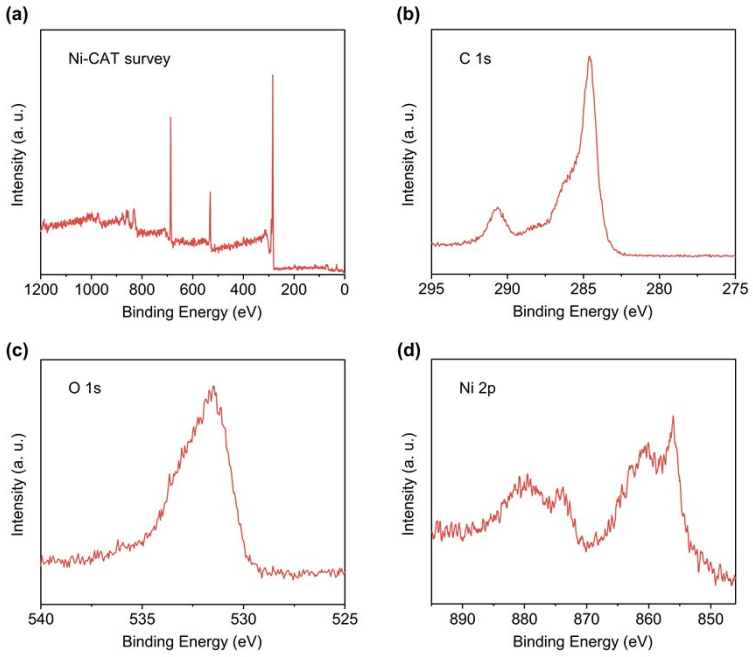

Fig. S8 XPS spectra of Ni-CAT. (a) Ni-CAT survey and the corresponding (b) C 1s, (c) O 1s and (d) Ni 2p region. Ni $2p_{3/2}$ peak has a binding energy of 856 eV, indicating the presence of Ni (II) in Ni-CAT.

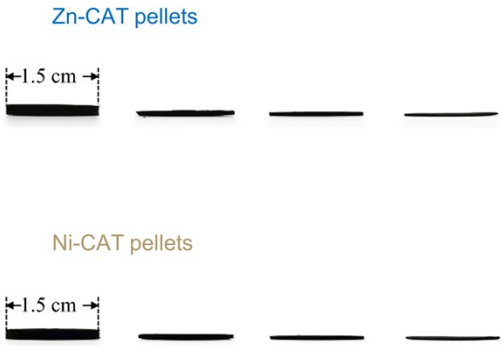

Fig. S9 Optic images of Zn/Ni-CAT pellets. The diameter of the pellets is 1.50 cm.

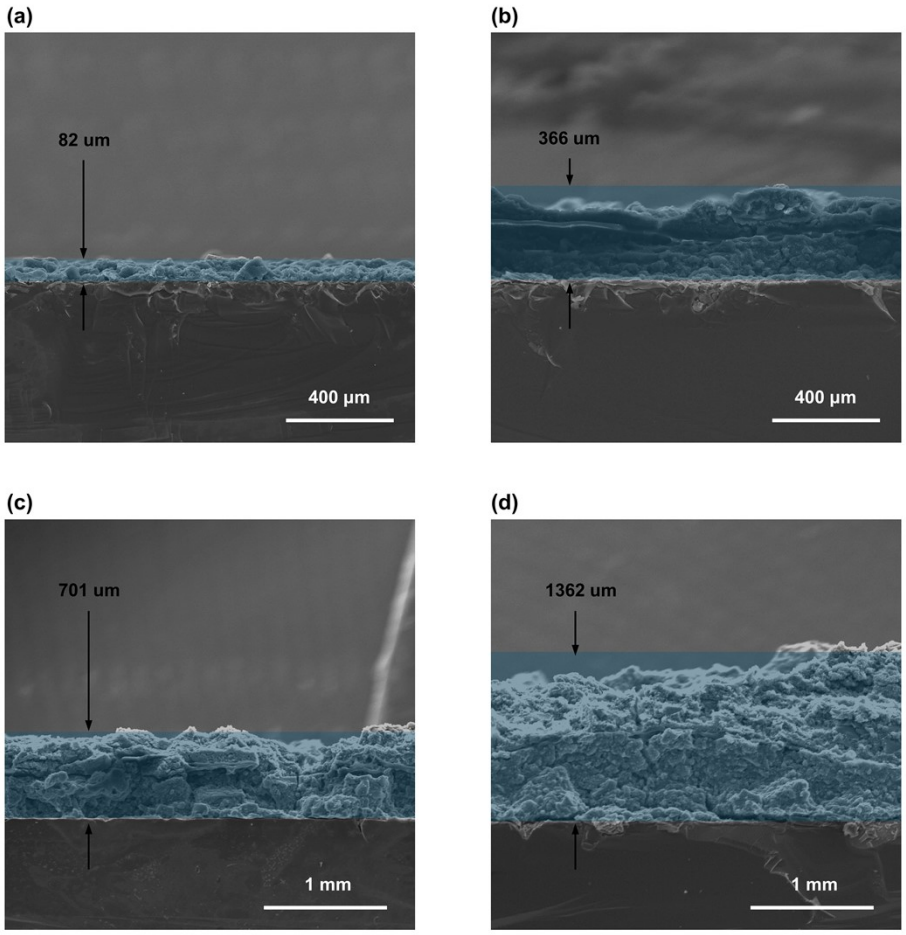

Fig. S10 SEM images of the Zn-CAT pellets. Pellets (diameter: 1.5 cm) with thicknesses of (a) 82 µm, (b) 366 µm, (c) 701 µm, and (d) 1362 µm were prepared. The measured weight for each pellet is 9.05 mg, 42.74 mg, 85.84 mg, and 172.74 mg. The calculated density for each pellet is 0.620 g cm^{-3}, 0.660 g cm^{-3}, 0.695 g cm^{-3}, and 0.720 g cm^{-3}.

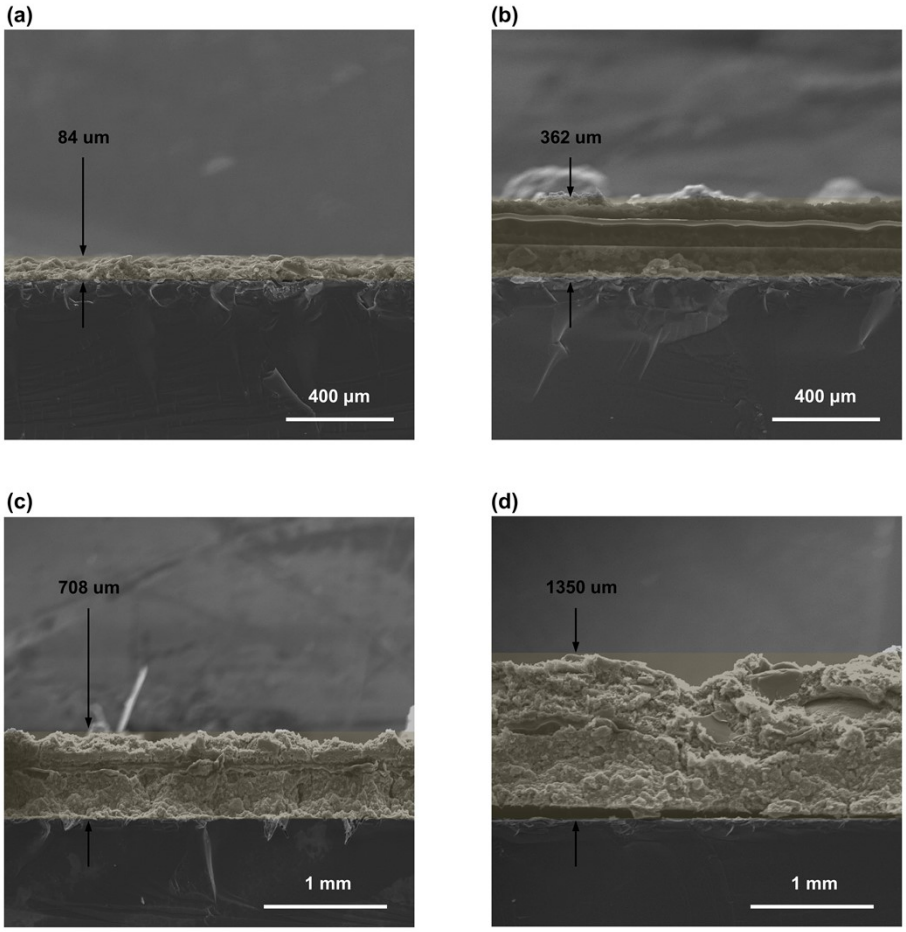

Fig. S11 SEM images of the Ni-CAT pellets. Pellets (diameter: 1.5 cm) with thicknesses of (a) 84 µm, (b) 362 µm, (c) 708 µm, and (d) 1350 µm were prepared. The measured weight for each pellet is 8.65 mg, 43.10 mg, 88.49 mg, and 173.62 mg. The calculated density for each pellet is 0.585 g cm^{-3}, 0.675 g cm^{-3}, 0.710 g cm^{-3}, and 0.730 g cm^{-3}.

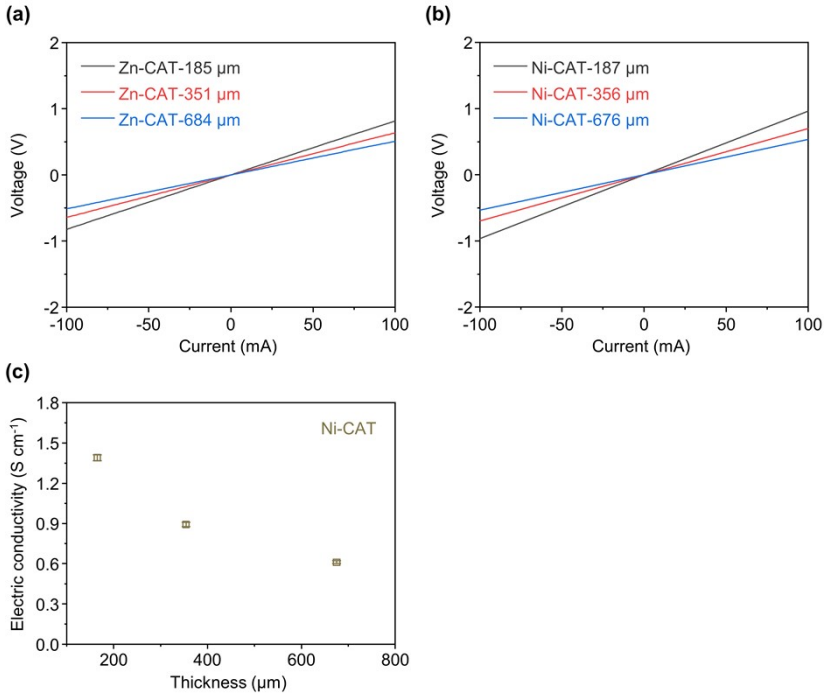

Fig. S12 Electrical conductivity measurement of Zn-CAT and Ni-CAT samples in pellets. Voltage-current curves of (a) Zn-CAT and (b) Ni-CAT, (c) calculated conductivity of Ni-CAT.

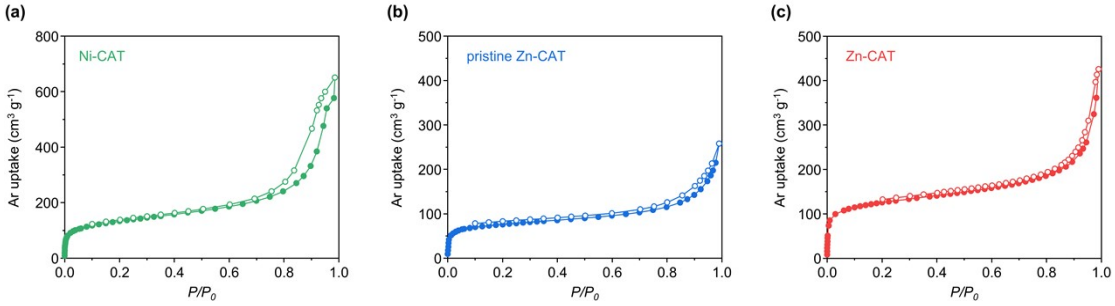

Fig. S13 Argon adsorption isotherms measured at 87 K. Adsorption and desorption points are represented by filled and empty circles, respectively. (a) Ni-CAT, (b) pristine Zn-CAT, (c) Zn-CAT.

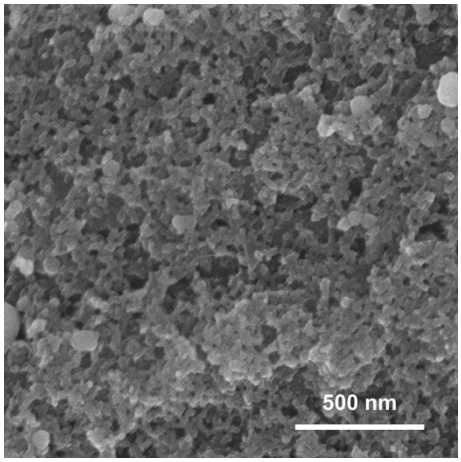

Fig. S14 SEM images of the Ni-CAT after 100 cycles.

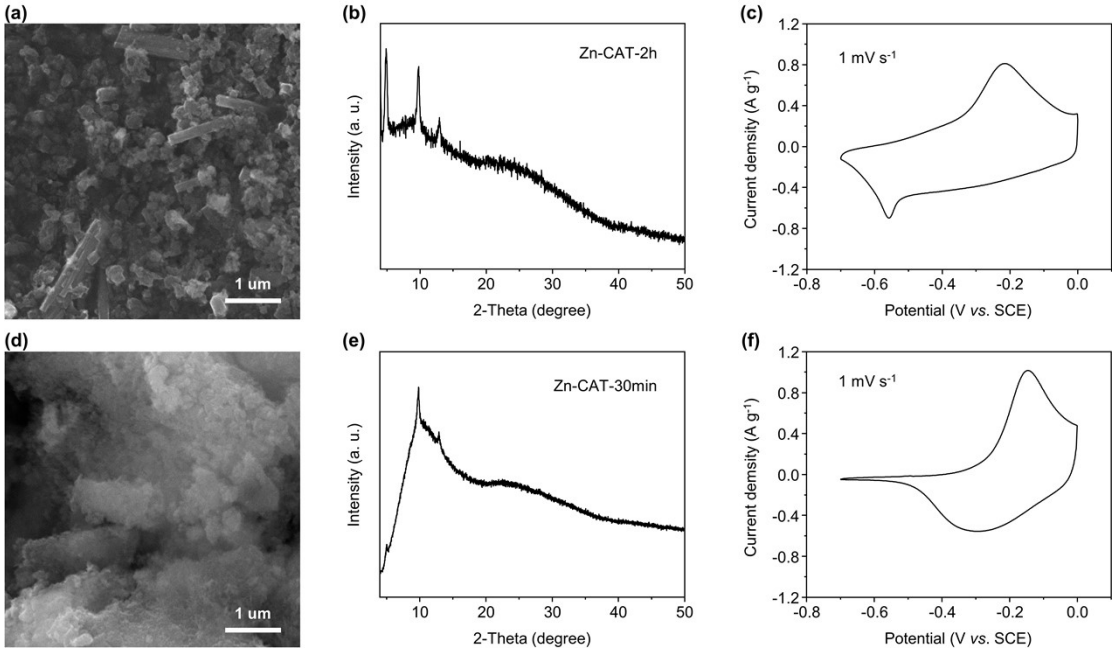

Fig. S15 (a) and (d), SEM images of Zn-CAT-1h and Zn-CAT-30min. (b) and (e), XRD patterns of Zn-CAT-1h and Zn-CAT-30min; (c) and (f) CV profiles collected with Zn-CAT-1h and Zn-CAT-30min.

To further validate this conclusion, we have obtained the Zn-CAT particles with different particle sizes by controlling the hydrothermal time of the Zn-CAT. As expected, the reduction peaks at high potentials gradually decreased with the decrease of the Zn-CAT particle size. However, low synthesis time may also lead to lower

sample crystallinity, which will greatly affect the electrochemical performance of the Zn-CAT electrode ground, as revealed in Fig. S15.

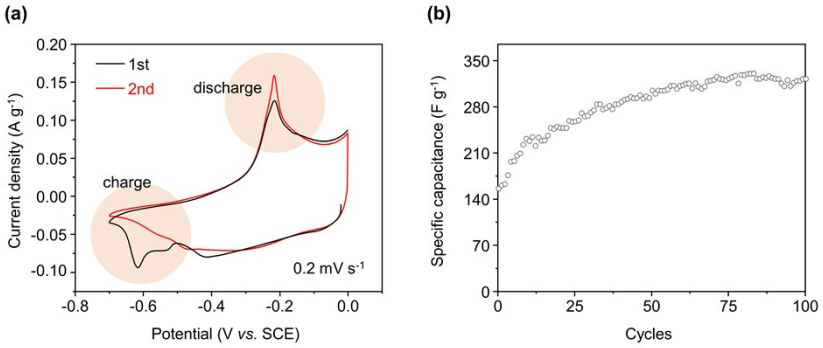

Fig. S16 The CV curves of the pristine Zn-CAT at 0.2 mV s^{-1}.

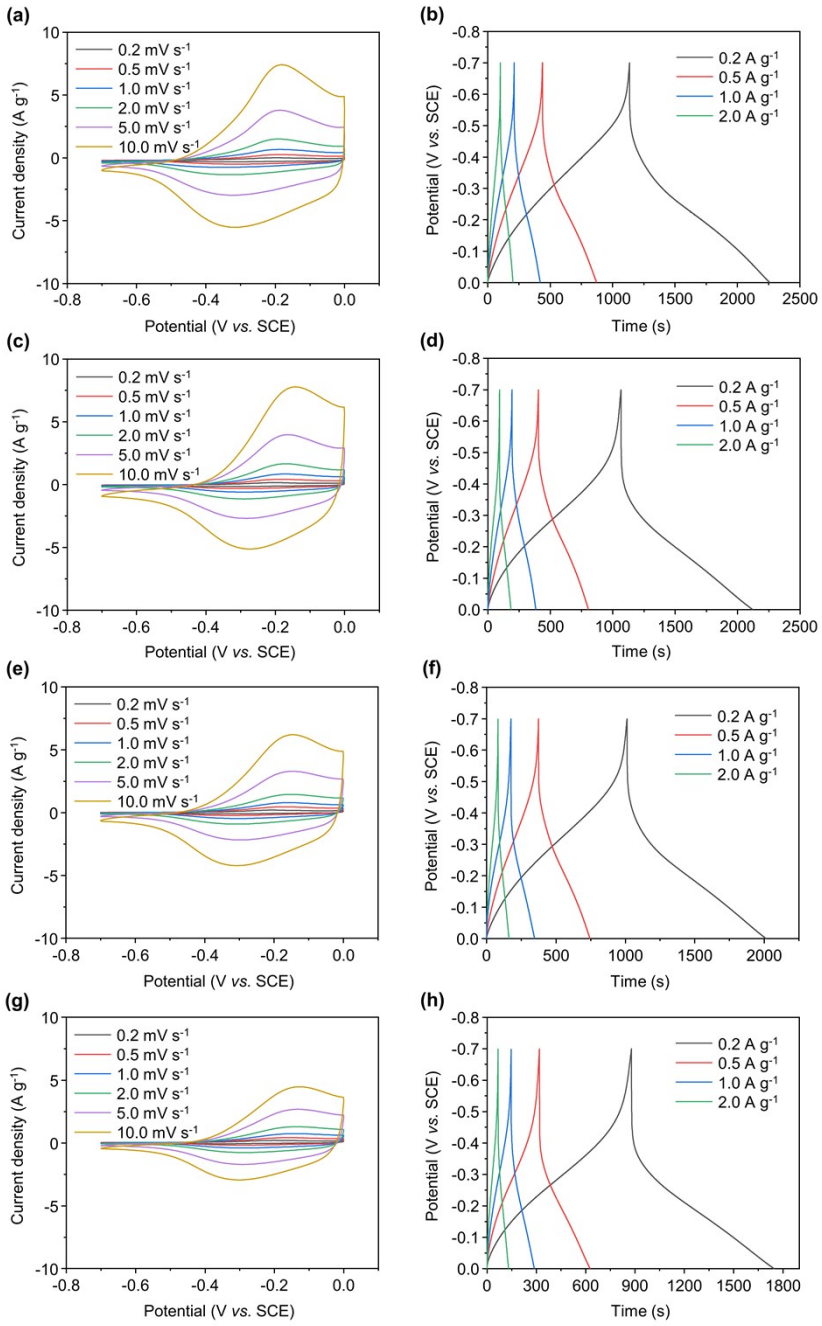

Fig. S17 Electrochemical performance of Zn-CAT pellet in 1 M Na_2SO_4. Cyclic voltammetry profiles collected with different electrode pellets of (a) 5.1 mg cm^{-2}, (c) 24.2 mg cm^{-2}, (e) 48.6 mg cm^{-2}, and (g) 97.8 mg cm^{-2} at different scan rates from 0.2 to 10 mVs^{-1}. Galvanostatic charge discharge profiles were collected with different electrode pellets of (b) 5.1 mg cm-2, (d) 24.2 mg cm-2, (f) 48.6 mg cm-2, and (h) 97.8 mg cm-2 at different current densities from 0.2 to 2.0 A g^{-1}.

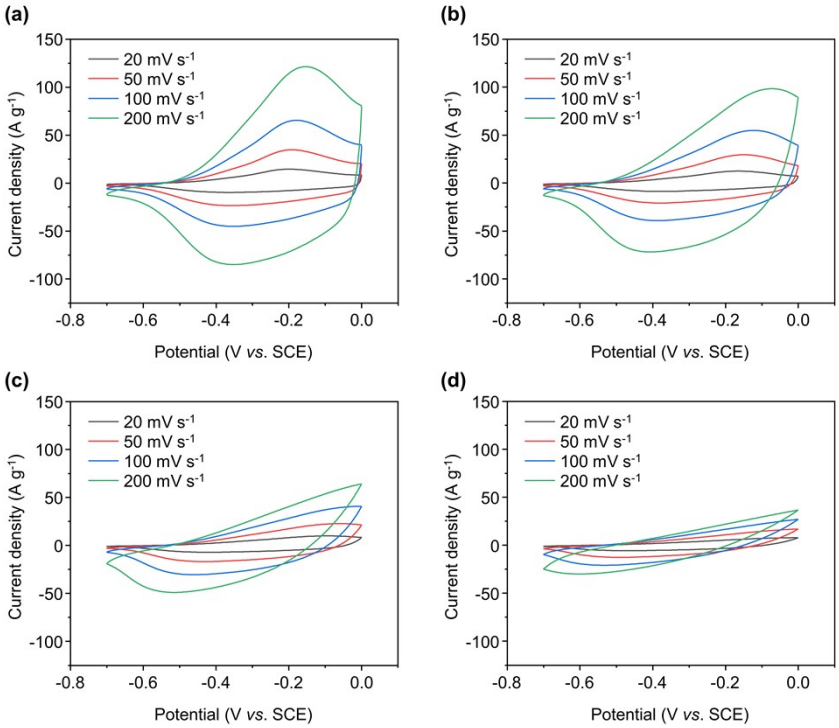

Fig. S18 Electrochemical performance of Zn-CAT pellet in 1 M Na_2SO_4 Cyclic voltammetry profiles collected with different electrode pellets of (a) 5.2 mg cm^{-2}, (b) 24.7 mg cm^{-2}, (c) 49.4 mg cm^{-2}, and (d) 97.4 mg cm^{-2} at different scan rates from 20 to 200 mVs^{-1}.

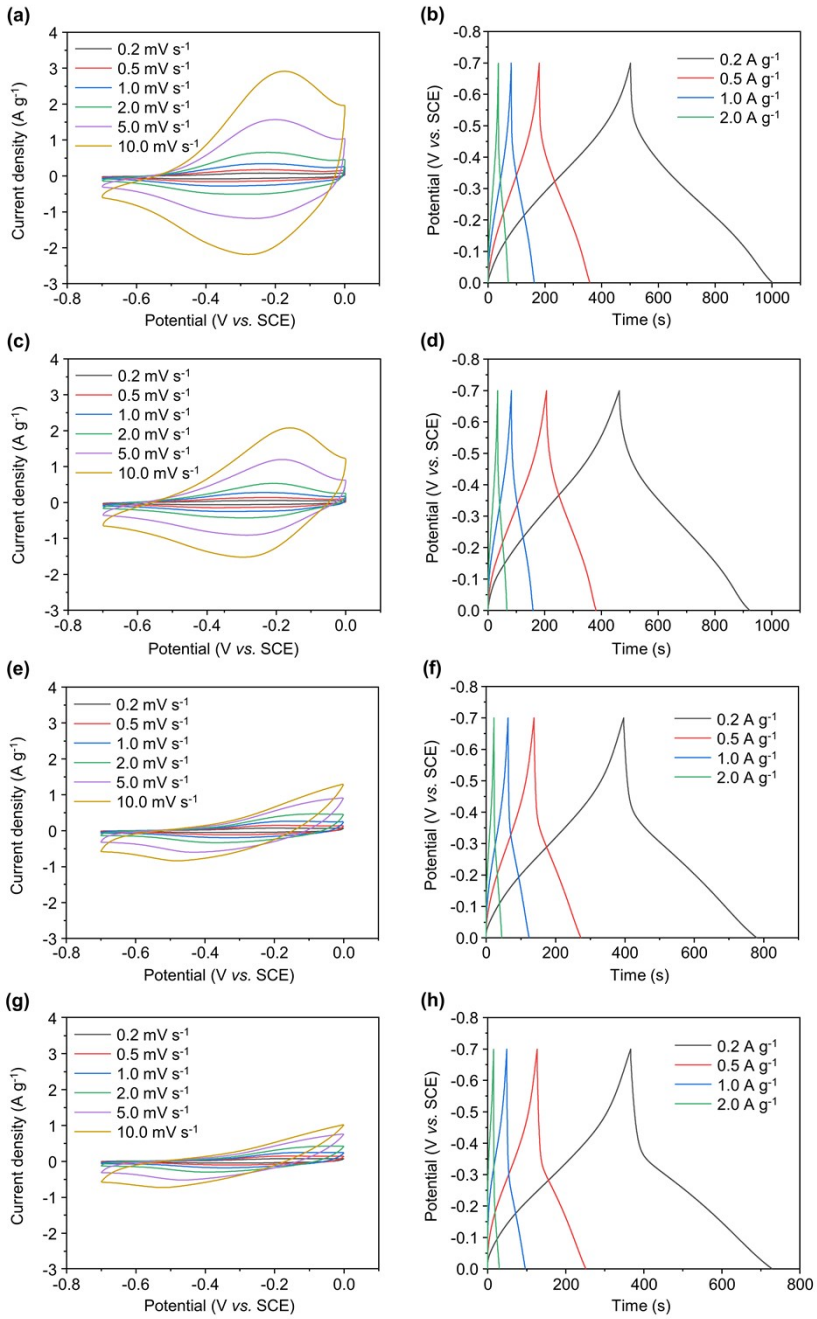

Fig. S19 Electrochemical performance of Ni-CAT pellet in 1 M Na_2SO_4. Cyclic voltammetry profiles collected with different electrode pellets of (a) 4.9 mg cm^{-2}, (c) 24.4 mg cm^{-2}, (e) 50.1 mg cm^{-2}, and (g) 98.3 mg cm^{-2} at different scan rates from 0.2 to 10 mVs^{-1}. Galvanostatic charge-discharge profiles were collected with different electrode pellets of (b) 4.9 mg cm-2, (d) 24.4 mg cm-2, (f) 50.1 mg cm-2, and (h) 98.3 mg cm-2 at different current densities from 0.2 to 2.0 A g^{-1}. With the increase of Ni-

CAT pellet thickness, the redox peaks of CV curves show a certain degree of shift, which is influenced by the kinetics.

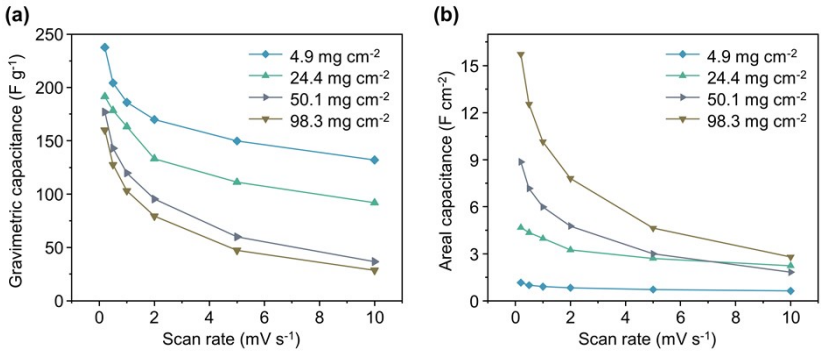

Fig. S20 Rate performance of Ni-CAT electrodes with difference areal densities. (a) Gravimetric rate performance for Ni-CAT pellet electrodes with different areal densities of 4.9, 24.4, 50.1 and 98.3 mg cm^{-2}. (b) Areal rate performance for the Ni-CAT pellet electrodes with different areal densities of 4.9, 24.4, 50.1 and 98.3 mg cm^{-2}.

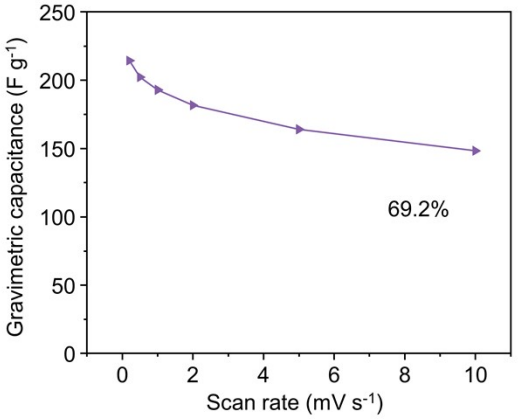

Fig. S21 Rate performance of pristine Zn-CAT.

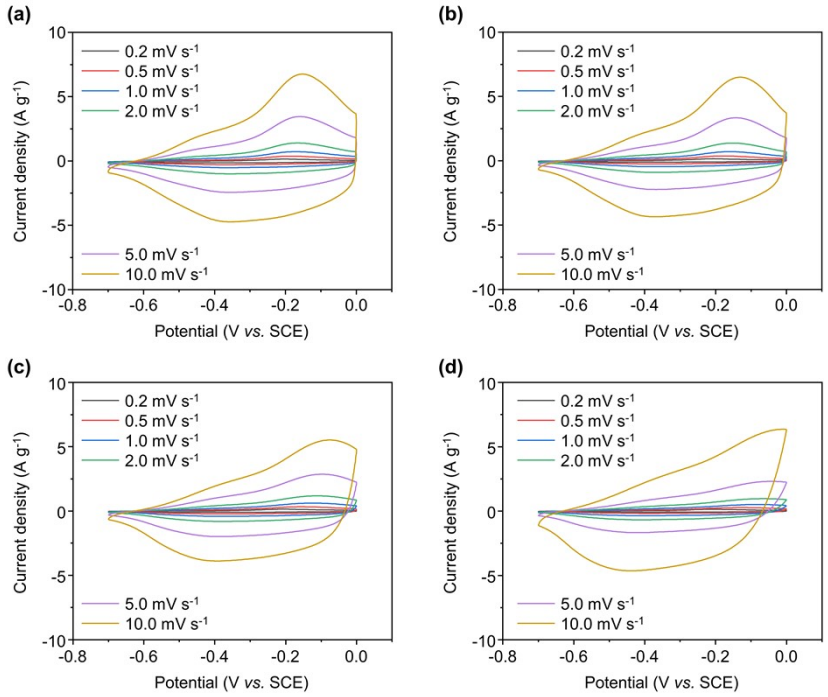

Fig. S22 Electrochemical performance of Zn-CAT pellet in 2 M NaOTf. Cyclic voltammetry profiles collected with different electrode pellets of (a) 5.2 mg cm^{-2}, (b) 24.7 mg cm^{-2}, (c) 49.4 mg cm^{-2}, and (d) 97.4 mg cm^{-2} at different scan rates from 0.2 to 10 mVs^{-1}.

Table S1. Rate performance of reported MOF-based electrode materials.

MOF-based electrode materials	Rate performance	Ref.
Zn-CAT	83.3% (from 0.2 to 10 mV s^{-1})	Our work
Cu-HATN	45.1% (from 0.15 to 1.5 A g^{-1})	1
$Ni_2[CuPc(NH)_8]$	43.8% (from 0.5 to 20 A g^{-1})	2
Ni-HAB	28.3% (from 0.2 to 100 mV s^{-1})	3
Cu-THQ	24.0% (from 0.05 to 1.0 A g^{-1})	4
HATN-SCu	30.2% (from 0.1 to 5.0 A g^{-1})	5
Cu-DBC	54.6% (from 0.2 to 10 A g^{-1})	6

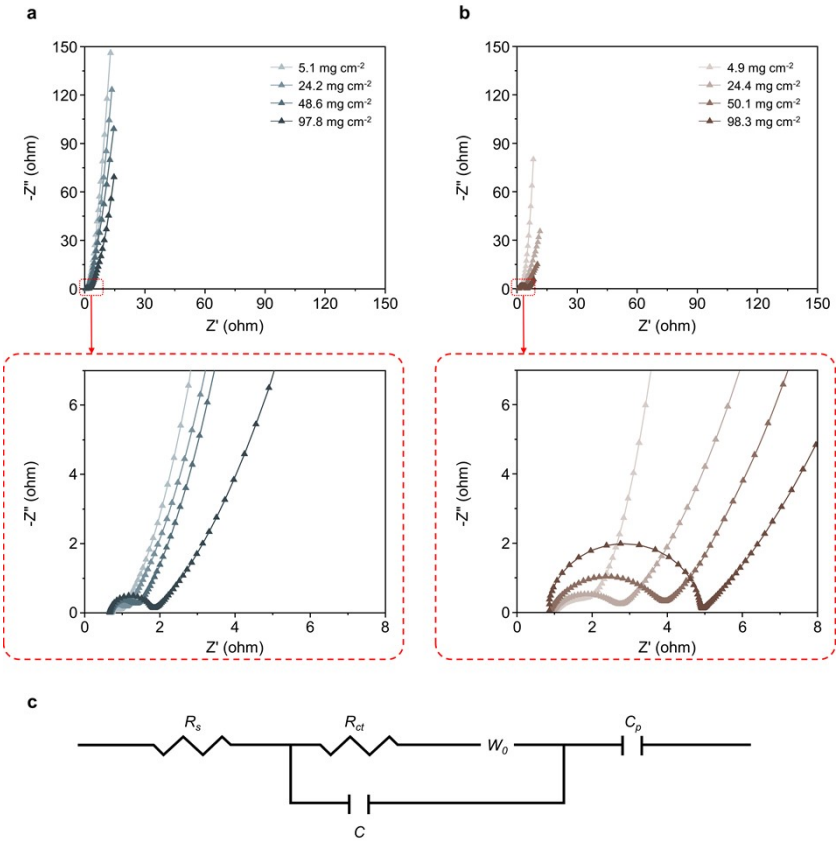

Fig. S23 Nyquist plots of Zn/Ni-CAT pellets electrode with different areal densities. Nyquist plots of (a) Zn-CAT pellets electrode with difference areal density (5.1, 24.2, 48.6 and 98.3 mg cm^{-2}), (b) Ni-CAT pellets electrode with difference areal density (4.9, 24.4, 50.1 and 97.8 mg cm^{-2}). (c) Equivalent circuit of Zn/Ni-CAT pellets electrodes. R_s is the equivalent ohmic resistance, C is electrical double-layer capacitance, W_o is the finite-length Warburg diffusion element, R_{ct} is charge transfer resistance, and C_p is the pseudocapacitance.

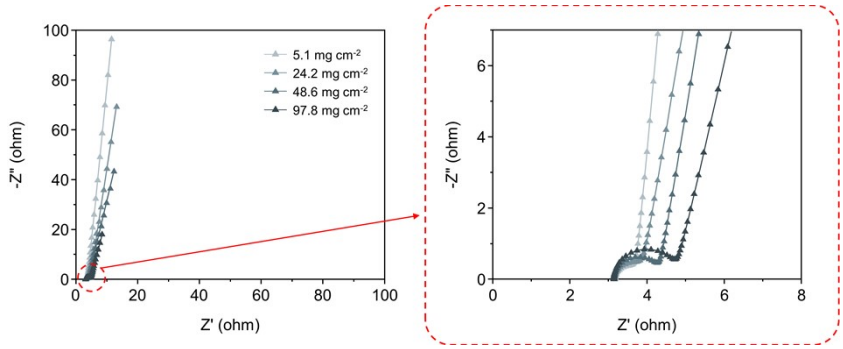

Fig. S24 Nyquist plots of Zn-CAT//MnO_2 ASC with different areal densities.

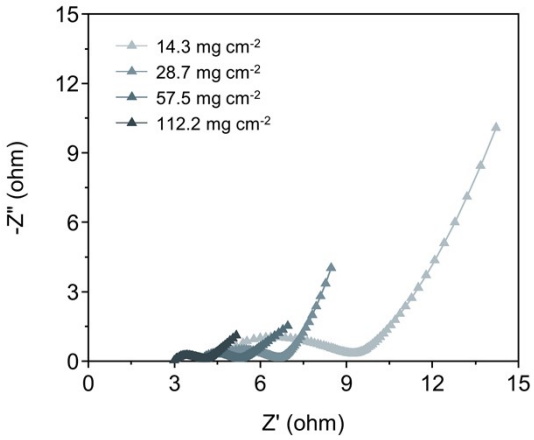

Fig. S25 Nyquist plots of AC-BC electrodes with different areal densities.

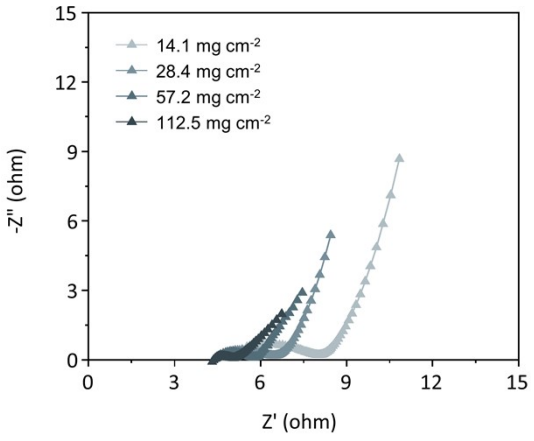

Fig. S26 Nyquist plots of YP-80F electrodes with different areal densities.

Table S2. Internal resistance (R_s) and charge-transfer resistance (R_{ct}) calculated from fitted EIS of AC-BC electrode and YP-80F electrode for different weight loadings in 1 M Na_2SO_4.

Different areal density	AC-BC(R_s)	AC-BC(R_{ct})	YP-80F(R_s)	YP-80F(R_{ct})
~14 mg	3.000 Ω	5.206 Ω	5.177 Ω	3.471 Ω
~28 mg	3.970 Ω	2.545 Ω	4.595 Ω	2.333 Ω
~56 mg	4.119 Ω	1.476 Ω	4.470 Ω	1.465 Ω
~112 mg	4.661 Ω	1.160 Ω	4.316 Ω	0.750 Ω

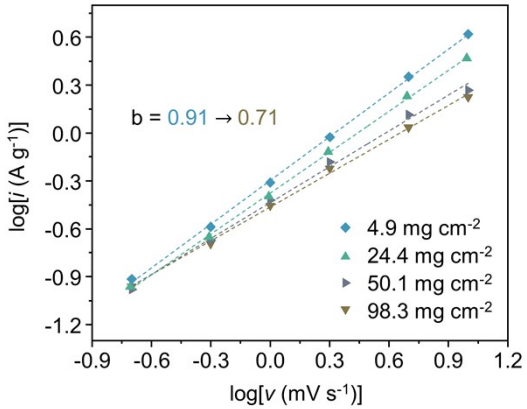

Fig. S27 Plot of the logarithm of Ni-CAT pellet electrode currents (i) versus the logarithm of scan rates (v) for the different areal densities of 4.9, 24.4, 50.1 and 98.3 mg cm^{-2}. The b-value is determined from the slope of the plots.

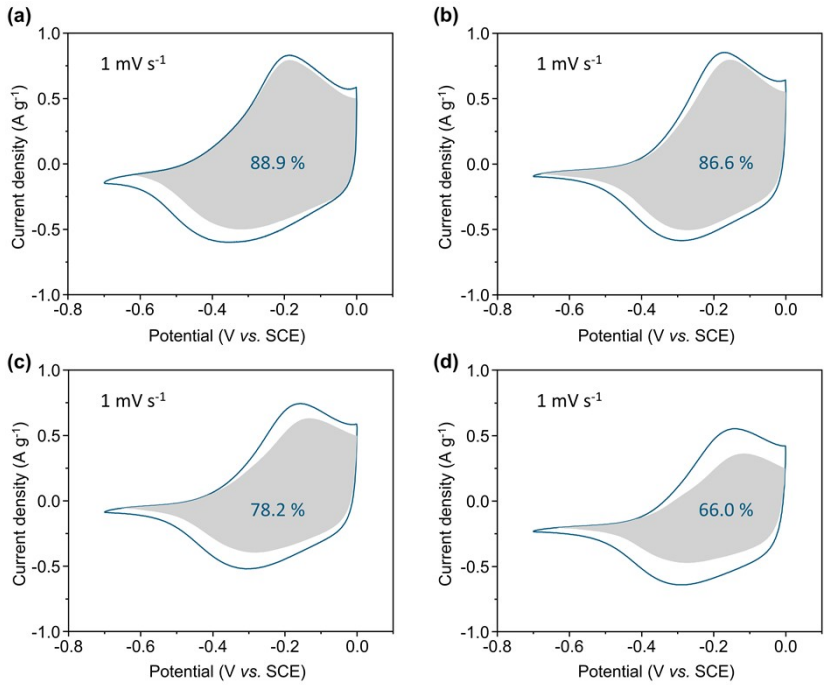

Fig. S28 Capacitive and diffusion currents contributed to the charge-storage of Zn-CAT electrode at 1 mV s^{-1} with different areal densities of 5.1, 24.2, 48.6 and 98.3 mg cm^{-2}. Two separate mechanisms, surface-controlled process (k_1v, including fast-response capacitive effect) and diffusion-controlled process ($k_2v^{1/2}$), contribute to the current response in CV curves at fixed potential according to the following equation: $i=k_1v+k_2v^{1/2}$, where i is the current, v is the scan rate. The fraction of current arising from two mechanisms at fixed potential can be distinguished by determining k_1 and k_2 values quantitatively.

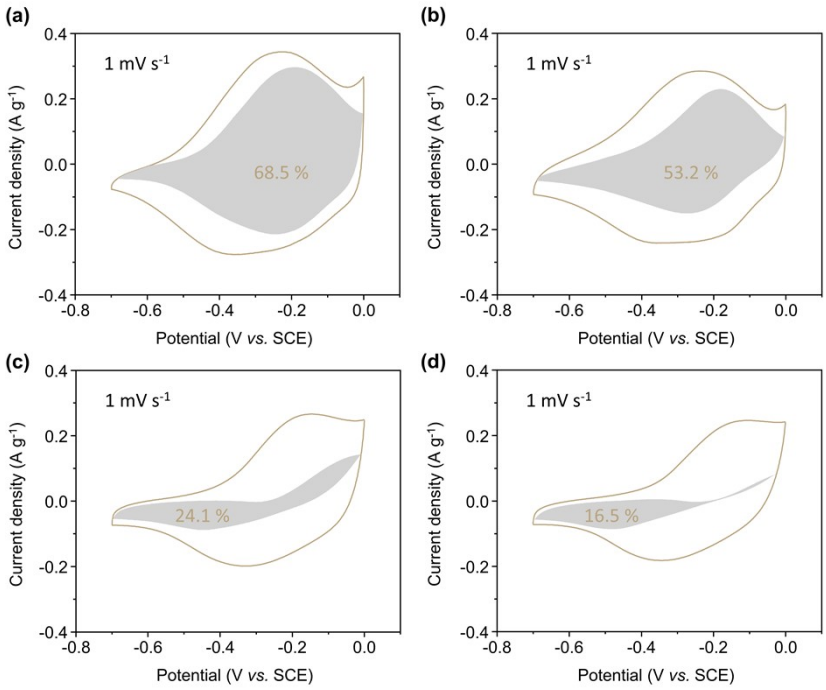

Fig. S29 Capacitive and diffusion currents contributed to the charge-storage of Zn-CAT electrode at 1 mV s^{-1} with different areal densities of 4.9, 24.4, 50.1 and 97.8 mg cm^{-2}.

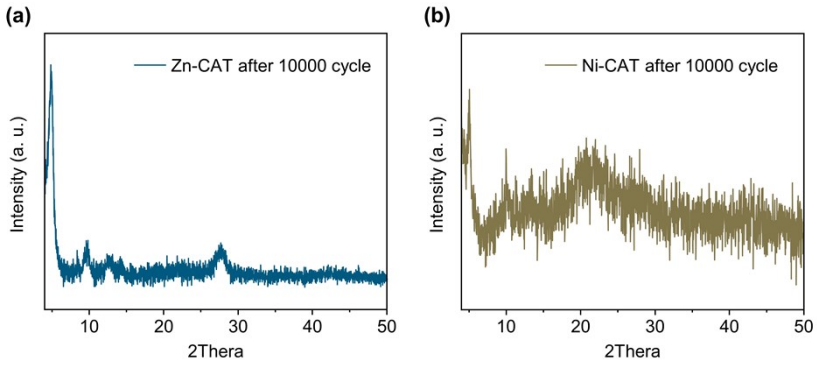

Fig. S30 PXRD patterns of the Zn- and Ni-CAT electrodes after 10000 cycles. As expected, Zn-CAT electrode still showed good structural stability after 10000 cycles. On the contrary, the XRD peak of Ni-CAT electrode weakened and disappeared after 10000 cycles indicated that the structure of Ni-CAT electrode might be destroyed during the cycling.

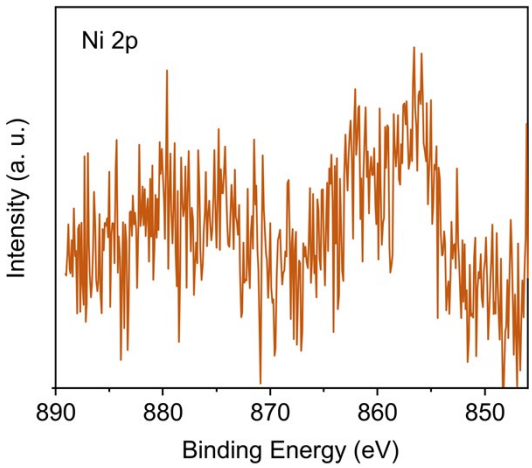

Fig. S31 Ni 2p region of Ni-CAT after 10000 cycles.

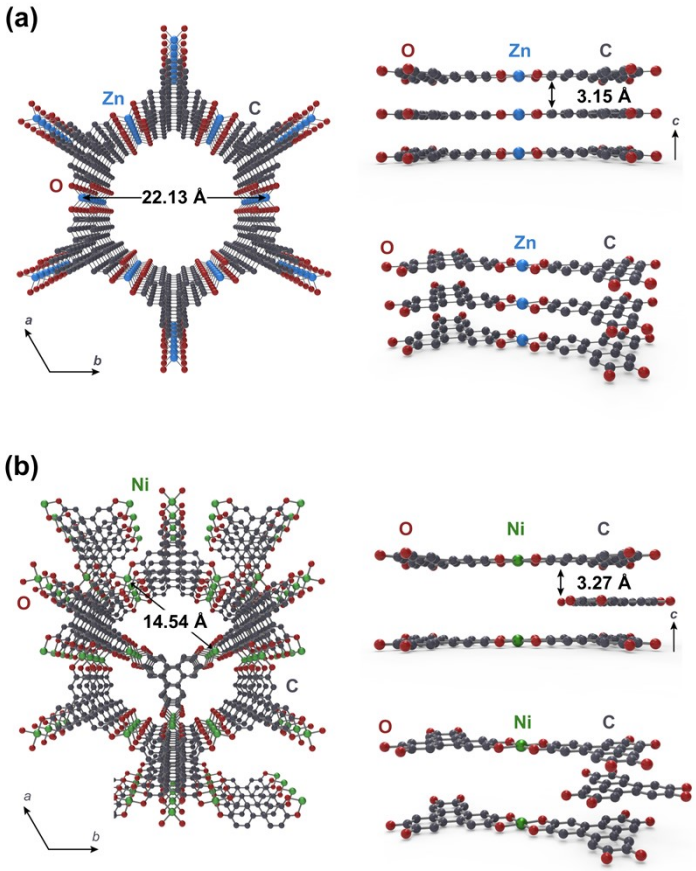

Fig. S32 Structural analysis of Zn-CAT and Ni-CAT. (a) and (b), A portion of the crystal structure along the c direction and views parallel to the ab plane for Zn-CAT and Ni-CAT. Hydrogen atoms are omitted for clarity.

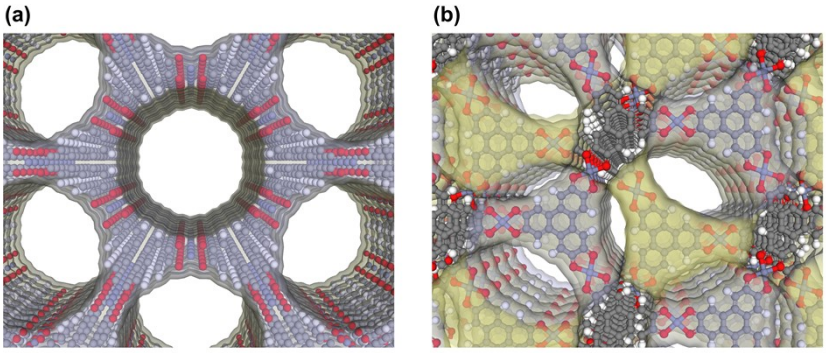

Fig. S33 Pore model of Zn-CAT and Ni-CAT.

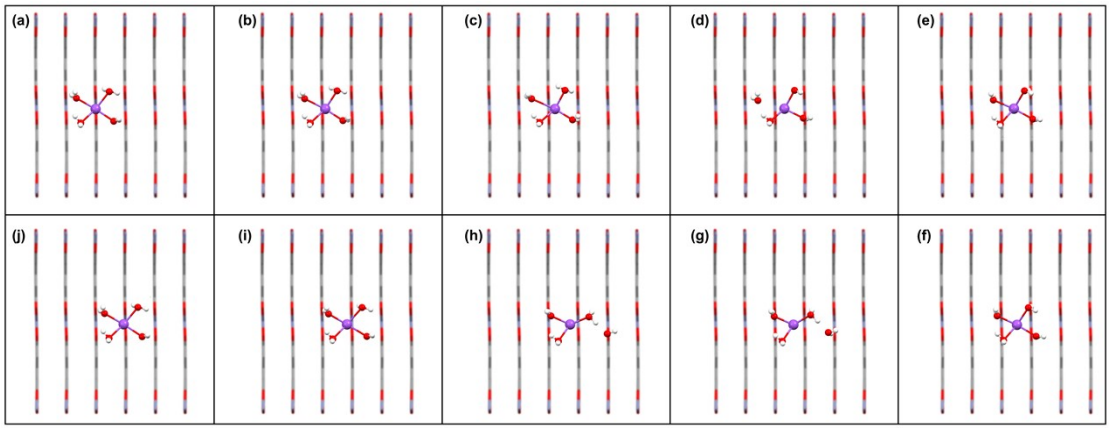

Fig. S34 Snapshots (a-j in time sequences) of hydrated Na^+ ions in AA-stacked Zn-CAT nanochannels.

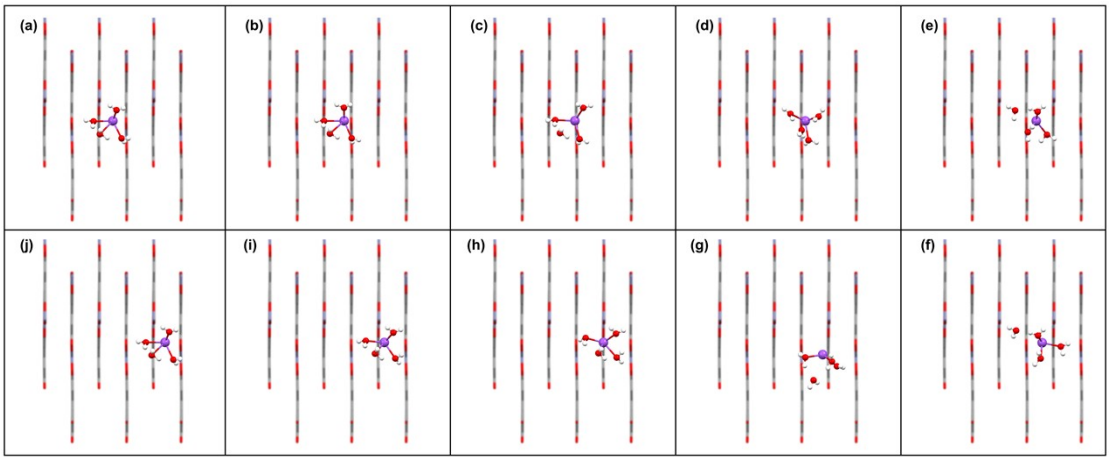

Fig. S35 Snapshots (a-j in time sequences) of hydrated Na^+ ions in AB-stacked Ni-CAT nanochannels.

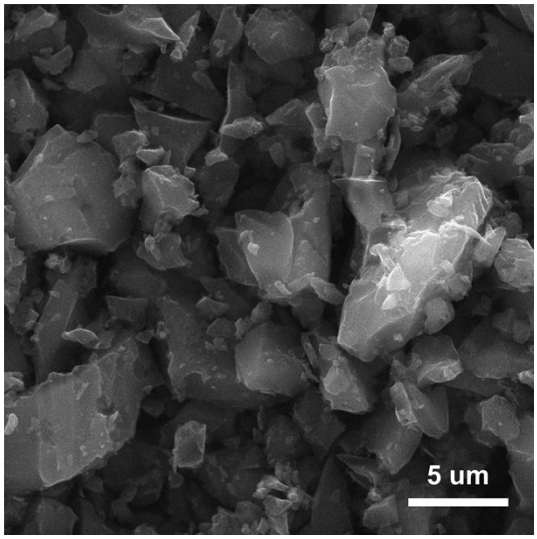

Fig. S36 SEM images of YP-80F, exhibiting different sizes and irregular shapes.

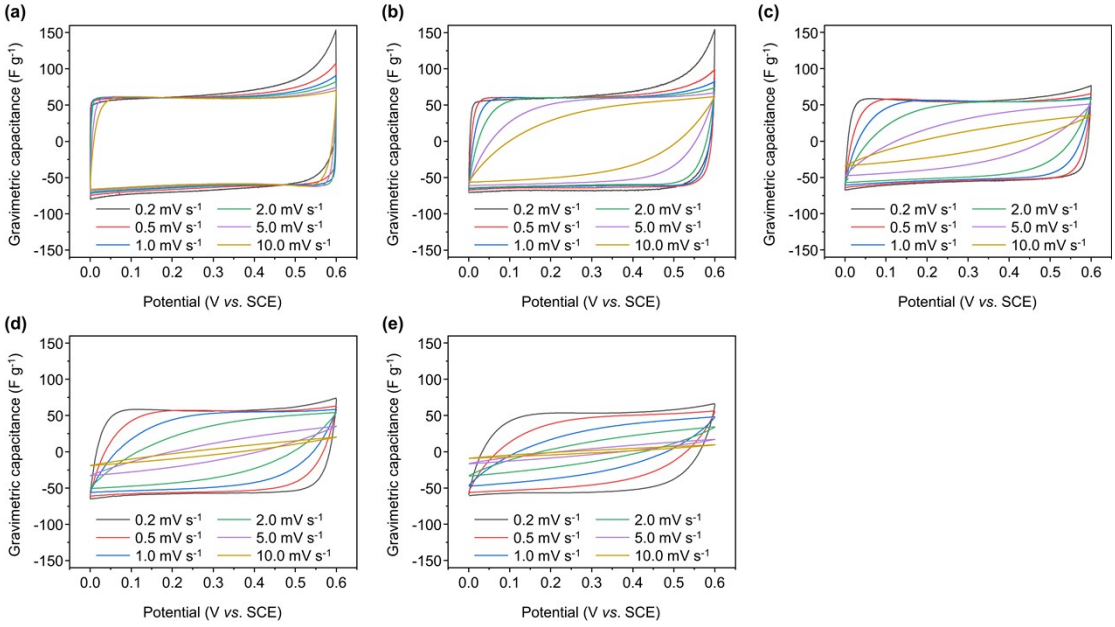

Fig. S37 Electrochemical performance of YP-80F pellets in 1 M Na_2SO_4. Cyclic voltammetry profiles collected with different electrode pellets of (a) 5.01 mg cm^{-2}, (b) 14.1 mg cm^{-2}, (c) 28.4 mg cm^{-2}, (d) 57.2 mg cm^{-2}, and (e) 112.5 mg cm^{-2} at different scan rates from 0.2 to 10 mV s^{-1}.

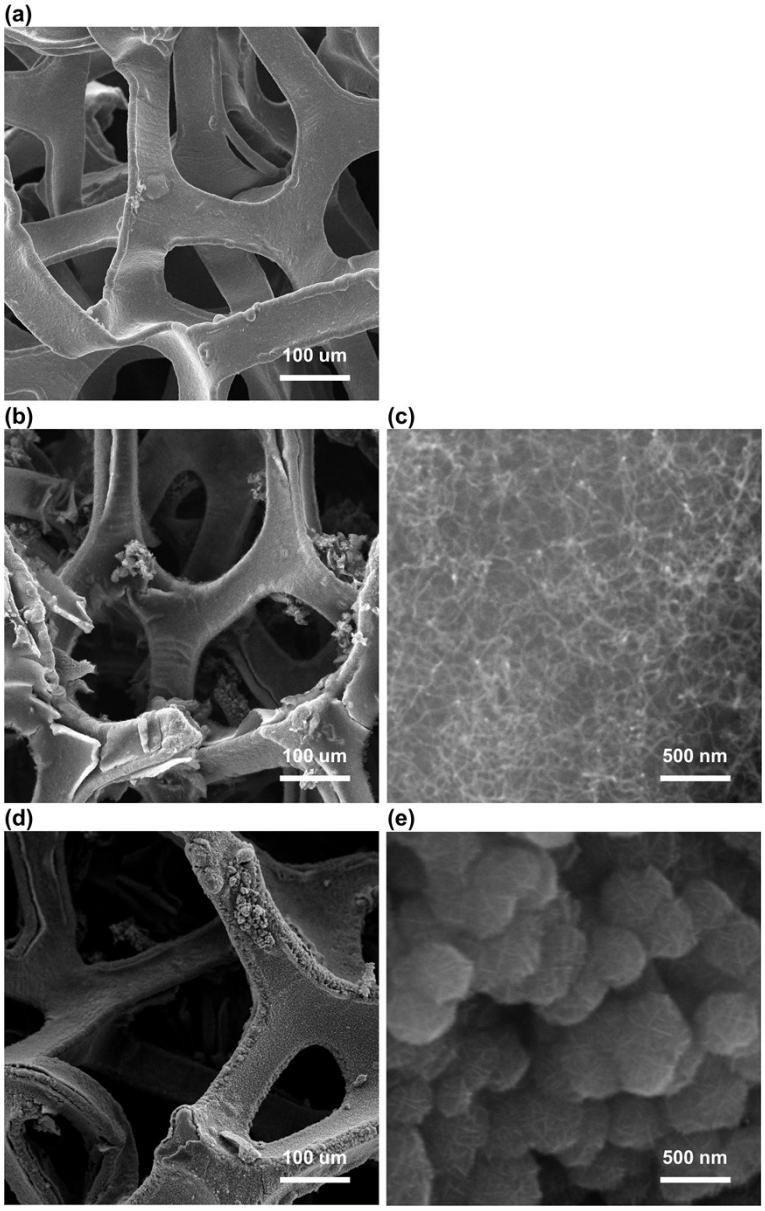

Fig. S38 SEM images of (a) nickel foam, (b) and (c) CNT@Ni foam, (d) and (e) MnO_2@CNT@Ni foam.

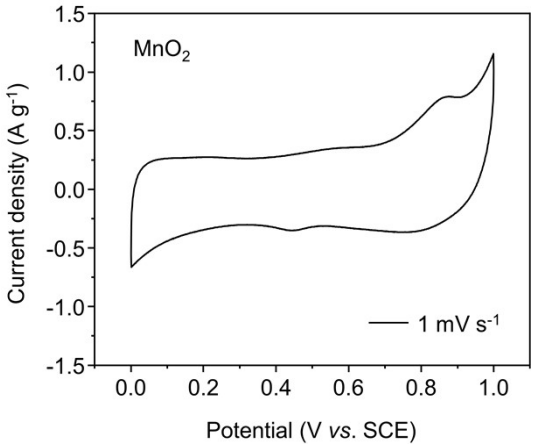

Fig. S39 Cyclic voltammetry profiles of MnO_2 electrode.

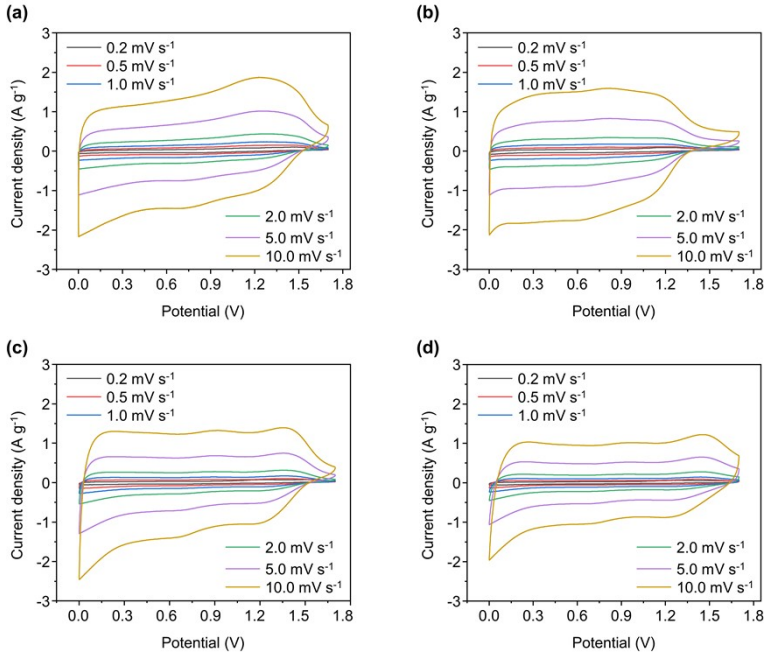

Fig. S40 Electrochemical performance of Zn-CAT//MnO_2 pellet in 1 M Na_2SO_4. Cyclic voltammetry profiles collected with different electrode pellets of (a) 5.1 mg cm^{-2} (MnO_2: 3.0 mg cm^{-2}), (b) 24.2 mg cm^{-2} (MnO_2: 15.1 mg cm^{-2}), (c) 48.6 mg cm^{-2} (MnO_2: 29.3 mg cm^{-2}), and (d) 97.8 mg cm^{-2} (MnO_2: 58.2 mg cm^{-2}) at different scan rates from 0.2 to 10 mVs^{-1}.

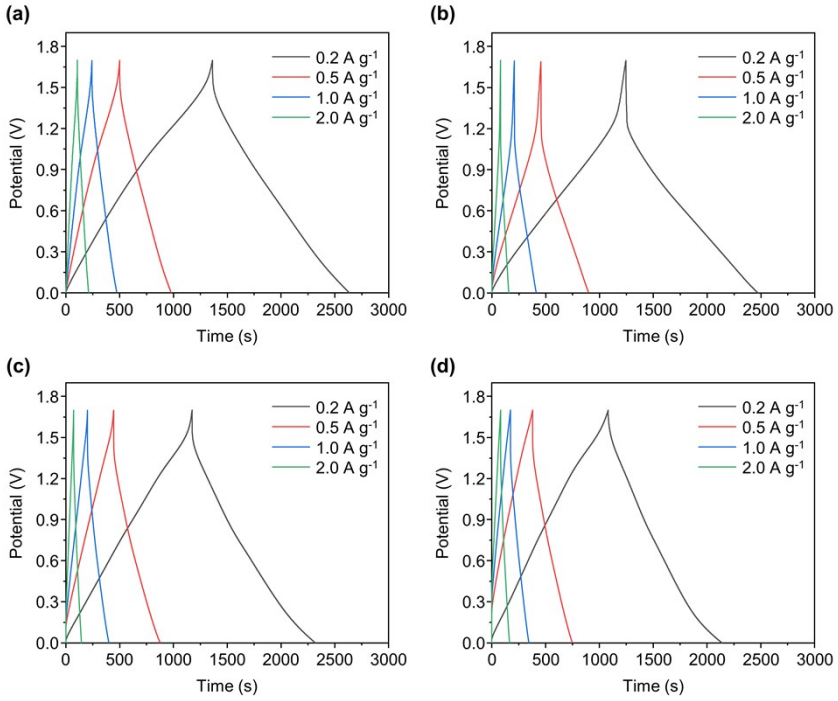

Fig. S41 Electrochemical performance of Zn-CAT//MnO_2 pellet in 1 M Na_2SO_4. Galvanostatic charge-discharge profiles were collected with different electrode pellets of (a) 5.1 mg cm^{-2} (MnO_2: 3.0 mg cm^{-2}), (b) 24.2 mg cm^{-2} (MnO_2: 15.1 mg cm^{-2}), (c) 48.6 mg cm^{-2} (MnO_2: 29.3 mg cm^{-2}), and (d) 97.8 mg cm^{-2} (MnO_2: 58.2 mg cm^{-2}) at different current densities from 0.2 to 2.0 A g^{-1}.

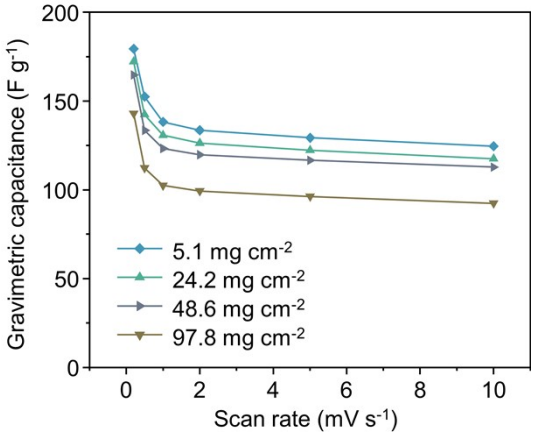

Fig. S42 Gravimetric rate performance for Zn-CAT//MnO_2 ASC with different areal densities of Zn-CAT (5.1, 24.2, 48.6, and 97.8 mg cm^{-2}).

The electrochemical properties of the asymmetric supercapacitors were evaluated in a typical two-electrode configuration with 1 M Na_2SO_4 electrolyte working in a

negative potential window of 0-1.7 V, and the results were displayed in Fig. S40. Zn-CAT electrodes use the same electrodes as the three-electrode test. Fig. S40 and S41 show representative CV curves and GCD curves for Zn-CAT//MnO_2 ASCs at different scan rates. The Zn-CAT//MnO_2 ASC delivers a mass-specific capacitance of 174 F g^{-1} at 0.2 mV s^{-1} (Fig. S40). Note that the mass-specific capacitance slightly decreases with increased thickness and mass loading, which is a common-seen phenomenon due to the limited atom economy in the bulk electrode. More impressively, even at a load of 97.8 g cm^{-2}, the specific capacitance of the Zn-CAT//MnO_2 ASCs possesses 141 F g^{-1}. Moreover, the Zn-CAT//MnO_2 ASCs still maintain a capacitance of 89 F g-1 when the scan rate increases by 50 times.

Reference

1. J. Yin, N. Li, M. Liu, Z. Li, X. Wang, M. Cheng, M. Zhong, W. Li, Y. Xu and X. H. Bu, *Adv. Funct. Mater.*, 2023, **33**, 2211950.
2. P. Zhang, M. Wang, Y. Liu, S. Yang, F. Wang, Y. Li, G. Chen, Z. Li, G. Wang, M. Zhu, R. Dong, M. Yu, O. G. Schmidt and X. Feng, *J. Am. Chem. Soc.*, 2021, **143**, 10168-10176.
3. D. Feng, T. Lei, M. R. Lukatskaya, J. Park, Z. Huang, M. Lee, L. Shaw, S. Chen, A. A. Yakovenko, A. Kulkarni, J. Xiao, K. Fredrickson, J. B. Tok, X. Zou, Y. Cui and Z. Bao, *Nat. Energy*, 2018, **3**, 30-36.
4. Q. Jiang, P. Xiong, J. Liu, Z. Xie, Q. Wang, X. Q. Yang, E. Hu, Y. Cao, J. Sun, Y. Xu and L. Chen, *Angew. Chem. Int. Ed.*, 2020, **59**, 5273-5277.
5. B. Wang, J. Li, M. Ye, Y. Zhang, Y. Tang, X. Hu, J. He and C. C. Li, *Adv. Funct. Mater.*, 2022, **32**.
6. J. Liu, Y. Zhou, Z. Xie, Y. Li, Y. Liu, J. Sun, Y. Ma, O. Terasaki and L. Chen, *Angew. Chem. Int. Ed.*, 2019, **59**, 1081-1086.
7. S. Zhang and N. Pan, *Adv. Energy Mater.*, 2014, **5**, 1401401.